Electrical Engineering
https://doi.org/10.1007/s00202-024-02839-1

ORIGINAL PAPER

SABO optimization algorithm-based backstepping controller for DSIG within a wind turbine system

Khaled Benzaoui[1] · Abderrahmen Bouguerra[1] · Samir Zeghlache[2] · Ahmed Elsanabary[3] · Saad Mekhilef[4,6] · Ahmed Bendib[5] · Loutfi Benyettou[1] · Keltoum Loukal[1]

Received: 22 July 2024 / Accepted: 29 October 2024

Abstract

Tuning the PI and backstepping (BS) controllers is a critical issue for ensuring good tracking performance and stable operation of the wind turbine based on dual-stator induction generator (WT-DSIG) systems. However, no existing research has yet comprehensively tuned the control parameters. Therefore, this paper proposes an innovative tuning method using the subtraction-average-based optimizer (SABO) to ensure optimal PI and backstepping controller parameters tuning. The optimally tuned controllers-based field-oriented control (FOC) scheme is applied for a WT-DSIG system. This research aims to offer an easy and effective method for optimal tuning of the control parameters, which contributes to improving the control performance, hence the WT-DSIG system's stability. The proposed method is superior to the existing techniques, as it uses the SABO, a metaheuristic stochastic algorithm, to simultaneously optimize the natural frequencies of the flux, speed, and current PI controllers and the backstepping controller's gains. To assess the effectiveness of the proposed control approach, a hardware-in-the-loop (HIL) implementation is carried out using the PLECS/RT-Box real-time simulator. The HIL findings through comparative study further confirm the superiority of the optimally designed controllers over the conventional techniques, highlighting significant enhancements in dynamic, steady state, THD, and time-integral performance criteria, ISE, and IAE.

Keywords Wind turbine · Dual-stator induction generator (DSIG) · Field-oriented control (FOC) · Backstepping (BS) control · Subtraction-average-based optimizer (SABO)

1 Introduction

Renewable energy (RE) is essential for sustainable development because it provides a limitless supply of clean electricity from natural sources like the sun, wind, water, and geothermal heat [1–3]. Wind energy is among the most significant

✉ Khaled Benzaoui
khaled.benzaoui@univ-msila.dz

Abderrahmen Bouguerra
abderrahmen.bouguerra@univ-msila.dz

Samir Zeghlache
samir.zeghlache@univ-msila.dz

Saad Mekhilef
smekhilef@swin.edu.au

Ahmed Bendib
ahmeddib28@gmail.com

Loutfi Benyettou
loutfi.benyettou@univ-msila.dz

Keltoum Loukal
keltoum.loukal@univ-msila.dz

[1] Electrical Engineering Laboratory (LGE), Electrical Engineering Department, Faculty of Technology, University of M'sila, 28000 M'sila, Algeria

[2] Signals and Systems Analysis Laboratory (LASS), Electronics Department, Faculty of Technology, University of M'sila, 28000 M'sila, Algeria

[3] Department of Electrical Engineering, Faculty of Engineering, Port Said University, Port Said 42526, Egypt

[4] School of Science, Computing and Engineering Technologies, Swinburne University of Technology, Hawthorn, VIC 3122, Australia

[5] SET Laboratory, Department of Electronics, University of Blida, Blida, Algeria

[6] Department of Electrical and Electronics Engineering, Presidency University, Bengaluru, Karnataka, India

Published online: 19 November 2024

forms of RE sources, and it generally uses turbines to create electricity. The effectiveness of wind energy is rising, and it can be used both on land and at sea, greatly assisting in supplying the world's energy demands [4–6]. In such systems, a generator is required to produce electrical energy from wind energy. One advanced type of electrical generator is the DSIG, which features a two-stator design, allowing for better control of the generated voltage and improved performance under variable load conditions [7, 8]. In the field of control, the field-oriented control (FOC) technique was widely adopted to control the DSIG [9]. However, tuning the controller parameters intended for DSIG with a multi-loop control strategy, including speed, flux, and stator currents, requires careful consideration to ensure optimal performance.

Several strategies were proposed to control DSIG, including traditional PID controllers, advanced controllers, and artificial intelligence (AI)-based control techniques. Among the advanced techniques are optimal sliding mode control (OSMC) [10], backstepping-SMC (BSMC) [11], super-twisting continuous SMC technique [12, 13], and nonlinear model predictive control (NMPC) [14]. In addition, AI techniques are presented by fuzzy logic (FL) and artificial neural networks (ANN) [15]. The PI and backstepping controllers are the most simple and easy-to-implement techniques used for the DISG and have shown satisfactory performance. For instance, the authors in [16] applied an FOC based on PI controllers for a DSIG within a grid-connected wind energy generation system considering variable speed. In [17], PI controllers-based stator FOC considering linear active disturbance rejection was suggested for a grid-connected WT-DSIG to achieve better tracking ability and dynamic performance. In [18], a dynamic current control strategy based on PI controllers with a reduced-order observer (ROO) has been proposed for a WT-DSIG system to reject the disturbances and enhance the current transient response. A PI regulators-based control approach with an instantaneous slip frequency control strategy was adopted to improve the rotor speed stability of wind turbines based on DSIG during simple power system faults [19]. In [20], the wind energy conversion system with a variable wind turbine speed connected to the grid based on DSIG was controlled using the backstepping control technique. In addition, a nonlinear backstepping control was proposed to control the WT-DSIG and offer better response time and overshoot performance compared to the conventional PI controller [21].

It is worth mentioning that all the research mentioned above did not address the tuning of the controllers' parameters except [22], which has determined the PI controllers' parameters by matching the characteristic equation of the system closed-loop models with the desired ones. Unfortunately, such a concept may not offer an appropriate tuning of the parameters for the multi-control loop structure and may also be challenging [21]. To this end, the authors in [23] used the genetic algorithm (GA) to facilitate parameter tuning compared to the "trial–error" method. However, while powerful for optimization, GA has several drawbacks, including high computational burdens and the inability to guarantee finding the global optimum.

To bridge this gap, an innovative tuning method based on the SABO algorithm is developed in this paper to ensure the ease and precision of setting parameters for PI and BS controllers. The designed controllers are applied to control the DSIG within a wind turbine system to improve its tracking performance and stability. The SABO is chosen in this work as it is a new metaheuristic algorithm with an improved exploitation phase and can effectively achieve global optima. The main contributions made in this paper are:

1) Applying the SABO to ensure ease and optimal tuning of the parameters of the flux, speed, and current control loops designed based on PI and BS controllers;
2) Establishing FOC technique based on the optimally tuned PI or BS controllers for a WT-DSIG system;
3) Implementing the designed controllers-based FOC technique in HIL using PLECS RT-Box to assess their performance compared to traditional PI and BS controllers.

The results show perfect tracking performance of the optimally tuned controllers, with low currents THD, less error and teeny ripples at steady state, and reduced values of ISE and IAE compared to the traditionally tuned controllers.

The rest of the paper is structured as follows: Section II presents the WT-DSIG system description and modeling. Section III describes the proposed control strategy. Section IV discusses the adopted SABO algorithm and its application to the WT-DSIG system control. Sections V and VI present the HIL results and discussion and the paper's conclusion.

2 WT-DSIG system description and modeling

2.1 System description

As shown in Fig. 1, the variable-speed wind system under study is built using a DSIG machine. The stator links the DSIG to the DC bus via two static converters, and the turbine drives it via a gearbox. The DSIG two fixed three-phase stator displaced with an electrical angle of 30° and a squirrel cage mobile rotor. This configuration provides advantages such as power segmentation, reduced rotor harmonic currents, and high reliability. In addition, according to this figure, the control scheme includes three main control loops, the rotor speed, rotor flux, and stators' currents. The speed controller is responsible for regulating the measured rotor speed

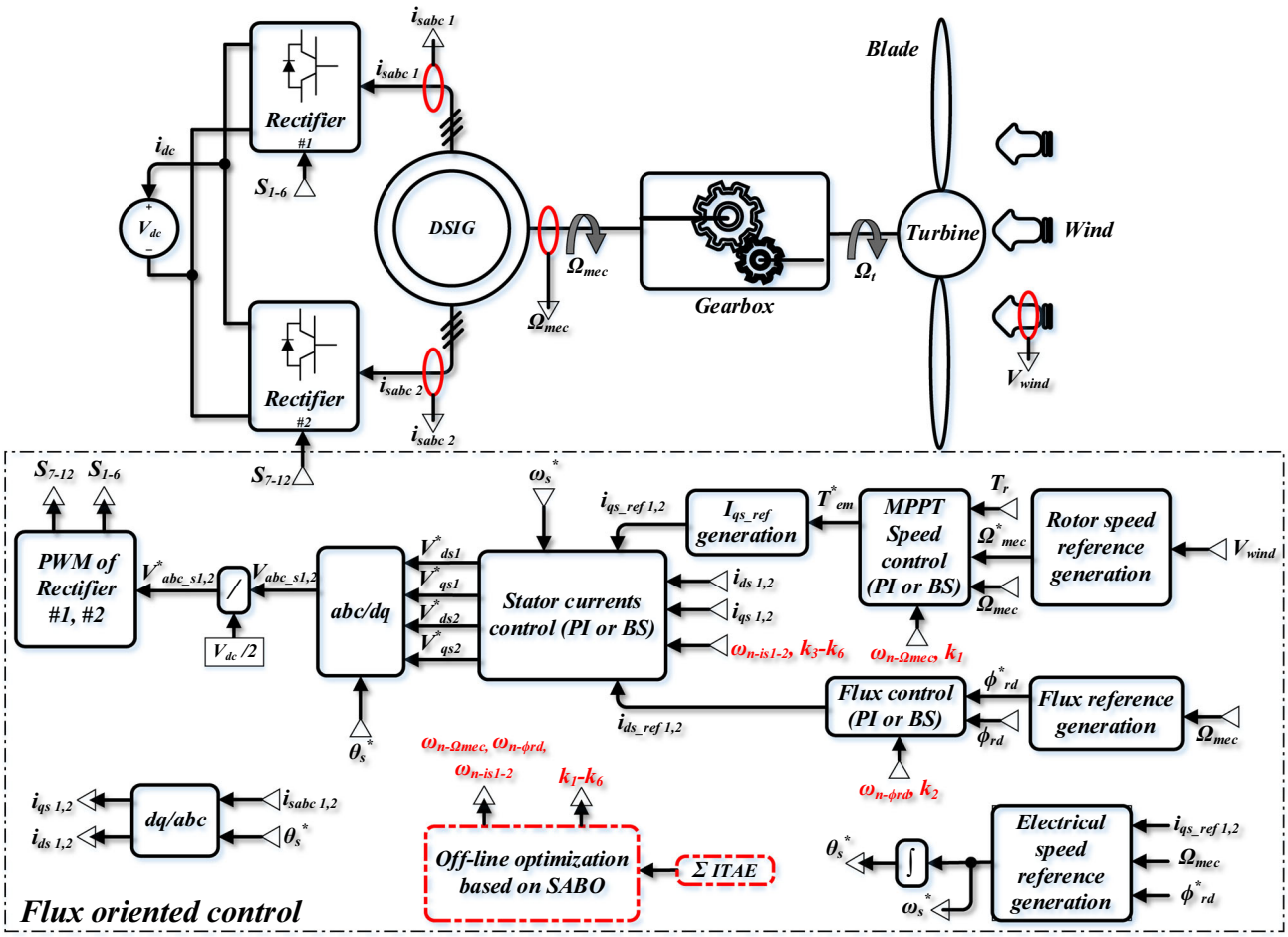

Fig. 1 WT-DSIG system with its designed control scheme

to its reference generated based on the wind speed. The flux controller is in charge of adjusting the actual flux to the obtained reference through a flux generator. The reference torque provided by the speed controller is used to generate the quadrature stators' current references, while the flux controller offers the direct stators' current references. The stator current controllers handle the errors between these generated current references and those obtained via the *abc* to *dq* transformation, which produces the converters' voltage references. The voltage references of the stators in the *abc* are passed through a PWM to generate the switches' commands.

It is worth mentioning that the three control loops are designed based on PI regulators first, while second, they are based on the BS technique. In addition, the natural frequencies of these controllers are optimally tuned offline by using a new metaheuristic SABO algorithm while considering the influence of each controller's response to others. In section III, more details and the mathematical modeling of each control stage will be given.

2.2 WT-DSIG system modeling

This subsection provides the mathematical modeling of all the elements integrated into the WT-DSIG system.

1) Wind Model: Wind constitutes the primary energy source harnessed by wind turbines [24]. In many studies, the wind is regarded as a stochastic variable defined by statistical parameters [25]. Notably, one approach in modeling wind involves generating its temporal characteristics by applying a transfer function to white noise. The determination of this transfer function is contingent upon the specific features of the location and the nature of the wind [1].

   The wind model is expressed through a Fourier series representation, portraying the wind as an amalgamation of various harmonics. This entails decomposing the wind speed into two components:

   - The wind's turbulent component, denoted as $V_t(t)$, defined by (2), is a stationary random process. It

exhibits constancy regardless of variations in the average wind speed, making it a crucial factor in wind modeling.

- A slow component V_{moy}, as in (1), is the average wind speed varying regularly over extended periods in a given site.

$$V_{wind}(t) = V_{moy} + V_t(t) \tag{1}$$

$$V_t(t) = \sum_{k=1}^{n} a_k \sin(\omega_k t) \tag{2}$$

where V_{wind} denotes the instantaneous wind speed, a_k is the amplitude of the harmonic of order k, ω_k represents the pulsation of the harmonic of order k, and n defines the rank of the last harmonic retained in the calculation of the wind profile.

Note that the aero turbine filters high-frequency variations. To do this, the turbulence component's low-pass filter (LPF) is reconstructed to replicate a more realistic characteristic, which transfer function is provided by:

$$G_f(s) = \frac{1}{1 + \delta s} \tag{3}$$

with:

$$\delta = \gamma \frac{R}{V_{moy}} \tag{4}$$

where γ is the rotor attenuation factor and R is the rotor diameter. Both may affect the value of the time constant δ [1].

2) Aerodynamics Modeling: The application of the wind with a velocity represented by V_{wind} to the wind turbine blades induces rotational motion, thereby generating mechanical power, P_t on the turbine shaft, expressed by:

$$P_t = 0.5 C_p(\lambda,\ \beta) \rho \pi R^2 V_{\text{wind}}^3 \tag{5}$$

where ρ is the density of air and λ is the tip speed ratio defined as a function of the wind and turbine speed, Ω_t, as follows:

$$\lambda = \frac{R\Omega_t}{V_{wind}} \tag{6}$$

Meanwhile, the power coefficient, C_p, is a metric for the aerodynamic efficiency inherent in the wind turbine and is contingent upon its specific characteristics. This coefficient is subject to a theoretical upper bound known as the Betz limit, set to 0.593, which still needs to be attainable in practical applications. Considering an estimated formulation, this power coefficient, C_p, can be expressed as a function of the blade angle β and relative velocity δ, as follows [26]:

$$C_p = 0.5109(116\delta - 0.4\beta - 5)e^{(-21\delta)} + 0.0068\lambda \tag{7}$$

with:

$$\delta = \frac{1}{\lambda + 0.08\beta} - \frac{0.035}{1 + \beta^3} \tag{8}$$

The gearbox synchronizes the rotational velocity of the wind turbine's slow shaft to the fast shaft of the DSIG. Assuming the gearbox to be ideal, with negligible mechanical losses, its behavior can be characterized by the following two expressions:

$$T_g = \frac{T_t}{G} \tag{9}$$

$$\Omega_t = \frac{\Omega_{mec}}{G} \tag{10}$$

while the shaft equation is given by:

$$\Omega_{\text{mec}} = \frac{1}{Js + k_f}(T_g - T_{em}) \tag{11}$$

In these equations, s is the Laplace operator, T_{em} represents the electromagnetic torque, T_t and T_g are the turbine torque and the DSIG torque, G is the gearbox gain, Ω_{mec} is the rotor mechanical speed, J is the moment of inertia, and k_f is the viscous coefficient.

At a specific operational state, the objective is to attain maximum mechanical power, indicative of the peak value of the power coefficient C_p. This is achieved when the relative velocity λ aligns with its optimal value, denoted as λ_{opt}, under the condition where the blade angle β is set to zero [26, 27].

3) DSIG Modeling: The DSIG has two stationary three-phase stator windings, each shifted by an electrical angle of 30°, and a movable squirrel cage rotor winding [21]. The electromagnetic torque is evaluated as:

$$T_{em} = P\left(\frac{L_m}{L_r + L_m}\right)\left[(i_{qs1} + i_{qs2})\phi_{rd} - (i_{ds1} + i_{ds2})\phi_{rq}\right] \tag{12}$$

By selecting the references associated with the rotating field, the DSIG model can be expressed more simply, as seen in the following concise manner.

$$\left[\dot{I}\right] = [L]^{-1}\{[B][V] - \omega_{sl}[C][I] - \{\omega_s[D_1] + [D_2]\}[I]\} \tag{13}$$

where P is the number of pole pairs, ω_s is the synchronous speed, ω_r is the rotor electrical angular speed, and ω_{sl} is the slip-speed expressed as follows:

$$\omega_{sl} = \omega_s - \omega_r \tag{14}$$

with: $\omega_r = P\Omega_{\text{mec}}$.
In addition, the matrices and vectors presented in (13) are defined as follows:

$$[I] = \begin{bmatrix} i_{ds1} & i_{qs1} & i_{ds2} & i_{qs2} & i_{dr} & i_{qr} \end{bmatrix}^T, \quad [V] = \begin{bmatrix} v_{ds1} & v_{qs1} & v_{ds2} & v_{qs2} & v_{dr} & v_{qr} \end{bmatrix}^T, \quad [B] = diag\begin{bmatrix} 1 & 1 & 1 & 1 & 0 & 0 \end{bmatrix}$$

$$[D_2] = diag\begin{bmatrix} R_{s1} & R_{s1} & R_{s2} & R_{s2} & R_r & R_r \end{bmatrix}$$

$$[C] = \begin{bmatrix} 0 & 0 & 0 & 0 & 0 & 0 \\ 0 & 0 & 0 & 0 & 0 & 0 \\ 0 & 0 & 0 & 0 & 0 & 0 \\ 0 & 0 & 0 & 0 & 0 & 0 \\ 0 & -L_m & 0 & -L_m & 0 & -(L_r + L_m) \\ L_m & 0 & L_m & 0 & L_r + L_m & 0 \end{bmatrix}$$

$$[L] = \begin{bmatrix} L_{s1} + L_m & 0 & L_m & 0 & L_m & 0 \\ 0 & L_{s1} + L_m & 0 & L_m & 0 & L_m \\ L_m & 0 & L_{s2} + L_m & 0 & L_m & 0 \\ 0 & L_m & 0 & L_{s2} + L_m & 0 & L_m \\ L_m & 0 & L_m & 0 & L_r + L_m & 0 \\ 0 & L_m & 0 & L_m & 0 & L_r + L_m \end{bmatrix}$$

$$[D_1] = \begin{bmatrix} 0 & -(L_{s1} + L_m) & 0 & -L_m & 0 & -L_m \\ (L_{s1} + L_m) & 0 & L_m & 0 & L_m & 0 \\ 0 & -L_m & 0 & -(L_{s2} + L_m) & 0 & -L_m \\ L_m & 0 & (L_{s2} + L_m) & 0 & L_m & 0 \\ 0 & 0 & 0 & 0 & 0 & 0 \\ 0 & 0 & 0 & 0 & 0 & 0 \end{bmatrix}$$

where L_m, L_r, L_{s1}, and L_{s2} are the inductance of magnetizing, rotor inductance, and stators, 1 and 2 inductances, respectively. R_r,R_{s1}, and R_{s2} are the resistances of the rotor and stators 1 and 2.

2.3 DC bus voltage mathematical formulation

In our case, the following formula is used to get the value of the DC bus, V_{dc} required to transfer a given power [28]:

$$V_{dc} = 2\sqrt{2}\alpha_1 E \tag{15}$$

where E is the RMS value of the grid voltage and α_1 is expressed by:

$$\alpha_1 = \sqrt{\frac{P_{\max} X^2}{9E^4} + 1} \tag{16}$$

where$X$ denotes the inductor impedance and P_{max} is the maximum generated power.

3 Proposed WT-DSIG control strategy

In this work, the rotor FOC strategy is adopted for the WT-DSIG system to allow autonomous control over the flux and electromagnetic torque by offering independent control of speed variation through the direct and quadrature stator currents.

After applying FOC to the DSIG model in (13), we conclude the following system of state equations:

$$\begin{cases} \dot{i}_{ds1} = \frac{1}{L_{s1}}\left\{v_{ds1} - R_{s1}i_{ds1} + \omega_s^*(L_{s1}i_{qs1} + \tau_r\phi_{rd}^*\omega_{sl}^*)\right\} \\ \dot{i}_{qs1} = \frac{1}{L_{s1}}\left\{v_{qs1} - R_{s1}i_{qs1} - \omega_s^*(L_{s1}i_{ds1} + \phi_{rd}^*)\right\} \\ \dot{i}_{ds2} = \frac{1}{L_{s2}}\left\{v_{ds2} - R_{s2}i_{ds2} + \omega_s^*(L_{s2}i_{qs2} + \tau_r\phi_{rd}^*\omega_{sl}^*)\right\} \\ \dot{i}_{qs2} = \frac{1}{L_{s2}}\left\{v_{qs2} - R_{s2}i_{qs2} - \omega_s^*(L_{s2}i_{ds2} + \phi_{rd}^*)\right\} \\ \dot{\phi}_{rd}^* = \mu(i_{ds1} + i_{ds2}) - \xi\phi_{rd} \\ \dot{\Omega}_{\text{mec}} = \frac{1}{J}\left(P\mu\phi_{rd}^*\left(i_{qs1} + i_{qs2}\right) - T_g - k_f\Omega_{mec}\right) \end{cases} \tag{17}$$

while τ, μ, and ξ are given by:$\tau = \frac{L_r}{R_r}$,$\mu = \frac{L_m}{L_m+L_r}$,$\xi = \frac{R_r}{L_m+L_r}$.

As shown in Fig. 1, the proposed FOC scheme includes three control loops, rotor speed, flux, and stators' currents, designed based on an optimally tuned controller using an optimization algorithm named SABO. The design of the three controllers is established based on two different control types, PI and BS, as detailed below.

3.1 PI controller-based control loop design

In this first case, the three control loops of the rotor speed, flux, and stators' currents are set up based on the PI regulator represented by the structure given in Fig. 2. Accordingly, the rotor output of the speed and flux controllers can be given by:

$$T_{em}^*(t) = k_{p-\Omega}\left(\Omega_{mec}^*(t) - \Omega_{mec}(t)\right) + k_{i-\Omega}\int\left(\Omega_{mec}^*(t) - \Omega_{mec}(t)\right)dt \tag{18}$$

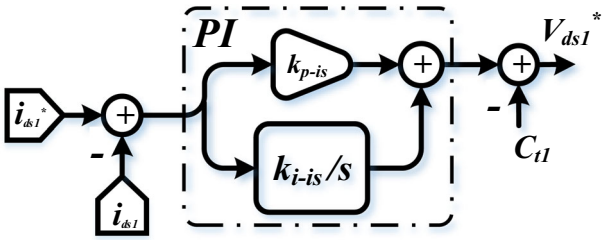

Fig. 2 PI controller-based current (i_{ds1}) control loop

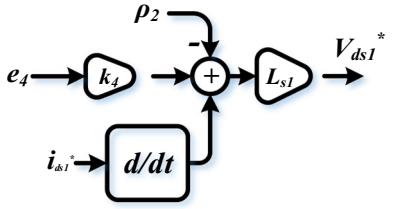

Fig. 3 BS controller-based current (i_{ds1}) control loop

$$i_{ds1,2}^*(t) = k_{p-\phi}\left(\phi_{rd}^*(t) - \phi_{rd}(t)\right) + k_{i-\phi}\int\left(\phi_{rd}^*(t) - \phi_{rd}(t)\right)dt \tag{19}$$

where $k_{p\text{-}\Omega}$, $k_{p\text{-}\phi}$, $k_{i\text{-}\Omega}$, and $k_{i\text{-}\phi}$ are the proportional and integral gains of the rotor speed and flux controllers, while Ω_{mec}^* and ϕ_{rd}^* are the rotor speed and flux references, respectively, which are generated by using the following expressions:

$$\Omega_{\text{mec}}^* = \frac{V_{\text{wind}}\lambda_{\text{opt}}G}{R} \tag{20}$$

$$\phi_{rd}^* = \begin{cases} \phi_{rd}^n & \text{if } \Omega_{\text{mec}} \le \Omega_{\text{mec}}^n \\ \frac{\Omega_r^n}{\Omega_r}\phi_{rd}^n & \text{if } \Omega_{\text{mec}} > \Omega_{\text{mec}}^n \end{cases} \tag{21}$$

where ϕ_{rd}^n is the rotor nominal flux, Ω_{mec} and Ω_{mec}^n are the rotor's mechanical speed and its nominal value.

On the other hand, by assuming that the reference currents in the two stators are the same, i.e., $i_{ds1}^* = i_{ds2}^*$ and $i_{qs1}^* = i_{qs2}^*$, the stator voltage references $v_{ds1,2}^*$ and $v_{qs1,2}^*$, generated by the current controllers can be expressed as follows:

$$\begin{cases} v_{ds1}^* = k_{p-is}\left(i_{ds1}^* - i_{ds1}\right) + k_{i-is}\int\left(i_{ds1}^* - i_{ds1}\right)dt - C_{t1} \\ v_{qs1}^* = k_{p-is}\left(i_{qs1}^* - i_{qs1}\right) + k_{i-is}\int\left(i_{qs1}^* - i_{qs1}\right)dt + C_{t2} \\ v_{ds2}^* = k_{p-is}\left(i_{ds2}^* - i_{ds2}\right) + k_{i-is}\int\left(i_{ds2}^* - i_{ds2}\right)dt - C_{t3} \\ v_{qs2}^* = k_{p-is}\left(i_{qs2}^* - i_{qs2}\right) + k_{i-is}\int\left(i_{qs2}^* - i_{qs2}\right)dt + C_{t4} \end{cases} \tag{22}$$

where $k_{p\text{-}is}$ and $k_{i\text{-}is}$ are the proportional and integral gains of the current controllers and the expressions of quadrature current references, i_{qs1}^* and i_{qs2}^*, and $C_{t1\text{-}4}$ are given by:

$$(i_{qs1}^* + i_{qs2}^*) = T_{em}^*\frac{L_m + L_r}{PL_m\phi_{rd}^*} \tag{23}$$

$$\begin{cases} C_{t1} = \omega_s^*(L_{s1}i_{qs1} + \tau_r\phi_{rd}^*\omega_{sl}^*) \\ C_{t2} = \omega_s^*(L_{s1}i_{ds1} + \phi_{rd}^*) \\ C_{t3} = \omega_s^*(L_{s2}i_{qs2} + \tau_r\phi_{rd}^*\omega_{sl}^*) \\ C_{t4} = \omega_s^*(L_{s2}i_{ds2} + \phi_{rd}^*) \end{cases} \tag{24}$$

where ω_s^* and ω_{sl}^* are the stator and slip-speed references expressed as follows:

$$\omega_{sl}^* = \frac{R_rL_m}{L_m + L_r}\frac{i_{qs1}^* + i_{qs2}^*}{\phi_{rd}^*} \tag{25}$$

$$\omega_s^* = \omega_{sl}^* + \omega_r \tag{26}$$

It is worth mentioning that the controllers' gains are related to the natural frequencies $\omega_{n\text{-}\Omega mec}$, $\omega_{n\text{-}\varphi rd}$, and $\omega_{n\text{-}is1,2}$ by the expressions defined below. These expressions are reached by matching the characteristic equations of the closed-loop transfer function with the desired second-order ones.

$$\begin{cases} k_{p-\Omega} = 2k_{si}\omega_{n-\Omega\text{mec}}J - k_f \\ k_{i-\Omega} = J\omega_{n-\Omega\text{mec}}^2 \end{cases}$$

$$\begin{cases} k_{p-\phi} = {(2(L_m+L_r)k_{si}\omega_{n-\phi rd}-R_r)}/{(R_rL_m)} \\ k_{i-\phi} = \left({(L_m+L_r)\omega_{n-\phi rd}^2}\right)/{(R_rL_m)} \end{cases}$$

$$\begin{cases} k_{p-is} = 2k_{si}\omega_{n-is1,2}L_{s1,2} - R_{s1,2} \\ k_{i-is} = L_{s1,2}\omega_{n-is1,2}^2 \end{cases}$$

where k_{si} is the damping factor set to $\frac{1}{\sqrt{2}}$.

3.2 Backstepping-based control loops design

This subsection discusses the three control loop design based on the BS, as presented in the structure of Fig. 3.

Defining the following errors and their derivatives are given as:

$$\begin{cases} e_1 = \Omega_{\text{mec}}^* - \Omega_{\text{mec}} \\ e_2 = \phi_{rd}^* - \phi_{rd} \end{cases} \tag{27}$$

$$\begin{cases} \dot{e}_1 = \dot{\Omega}_{\text{mec}}^* - \dot{\Omega}_{\text{mec}} \\ \dot{e}_2 = \dot{\phi}_{rd}^* - \dot{\phi}_{rd} \end{cases} \tag{28}$$

From the system of Eqs. (17) and (29), we conclude:

$$\begin{cases} \dot{e}_1 = \dot{\Omega}^*_{\text{mec}} - \frac{1}{J}\left(P\mu\phi^*_{rd}\left(i_{qs1}+i_{qs2}\right) - T_g - k_f\Omega_{\text{mec}}\right) \\ \dot{e}_2 = \dot{\phi}^*_{rd} - \mu(i_{ds1}+i_{ds2}) - \xi\phi_{rd} \end{cases} \tag{29}$$

The first Lyapunov function, v_1, and its derivative are given as:

$$v_1 = \frac{1}{2}(e_1^2 + e_2^2) \tag{30}$$

$$\dot{v}_1 = e_1\,\dot{e}_1 + e_2\,\dot{e}_2 \tag{31}$$

From the system of Eqs. (29), we can rewrite the derivative of v_1 as follows:

$$\begin{aligned} \dot{v}_1 =& e_1\left[\dot{\Omega}^*_{\text{mec}} - \frac{1}{J}\left[P\mu\phi^*_{rd}(i_{qs1}+i_{qs2}) - T_g - k_f\Omega_{\text{mec}}\right]\right] \\ &+ e_2\left[\dot{\phi}^*_{rd} - \mu(i_{ds1}+i_{ds2}) - \xi\phi_{rd}\right] \end{aligned} \tag{32}$$

To achieve stability according to Lyapunov theory, the derivative of $\dot{v}_1$ must always be negative ($\dot{v}_1 < 0$), in this case, we take:

$$\begin{cases} \dot{e}_1 = -k_1 e_1 \\ \dot{e}_2 = -k_2 e_2 \end{cases} \tag{33}$$

where k_1 and k_2 are positive constants,

From the system of Eq. (33), we can rewrite the system of Eq. (29) as follows:

$$\begin{cases} \dot{\Omega}^*_{\text{mec}} - \frac{1}{J}\left[P\mu\phi^*_{rd}(i_{qs1}+i_{qs2}) - T_g - k_f\Omega_{\text{mec}}\right] = -k_1 e_1 \\ \dot{\phi}^*_{rd} - \left(\mu\left(i_{ds1}+i_{ds2}\right) - \xi\phi_{rd}\right) = -k_2 e_2 \end{cases} \tag{34}$$

We consider i_{ds} and i_{qs} as virtual commands of our first subsystem by asking:

$$\begin{cases} i_{qs1} + i_{qs2} = i^*_{qs1} + i^*_{qs2} = i^*_{qs} \\ i_{ds1} + i_{ds2} = i^*_{ds1} + i^*_{ds2} = i^*_{ds} \end{cases} \tag{35}$$

Finally, the virtual order elements are given by:

$$\begin{cases} i^*_{qs1} + i^*_{qs2} = \frac{1}{P\mu\varphi^*_{rd}}\left[J\left(k_1 e_1 + \dot{\Omega}^*_{\text{mec}}\right) + T_r + k_f\Omega_{\text{mec}}\right] \\ i^*_{ds1} + i^*_{ds2} = \frac{1}{\mu}\left[k_2 e_2 + \dot{\phi}^*_{rd} + \xi\phi_{rd}\right] \end{cases} \tag{36}$$

On the other hand, considering the definition of the following errors and their derivatives:

$$\begin{cases} e_3 = i^*_{qs1} - i_{qs1} \\ e_4 = i^*_{ds1} - i_{ds1} \\ e_5 = i^*_{qs2} - i_{qs2} \\ e_6 = i^*_{ds2} - i_{ds2} \end{cases} \tag{37}$$

$$\begin{cases} \dot{e}_3 = \dot{i}^*_{qs1} - \dot{i}_{qs1} \\ \dot{e}_4 = \dot{i}^*_{ds1} - \dot{i}_{ds1} \\ \dot{e}_5 = \dot{i}^*_{qs2} - \dot{i}_{qs2} \\ \dot{e}_6 = \dot{i}^*_{ds2} - \dot{i}_{ds2} \end{cases} \tag{38}$$

From the system of Eq. (17), the system of Eq. (38) becomes:

$$\begin{cases} \dot{e}_3 = \dot{i}^*_{qs1} - \frac{1}{L_{s1}}\left\{v_{qs1} - R_{s1}i_{qs1} - \omega^*_s(L_{s1}i_{ds1} + \phi^*_{rd})\right\} \\ \dot{e}_4 = \dot{i}^*_{ds1} - \frac{1}{L_{s1}}\left\{v_{ds1} - R_{s1}i_{ds1} + \omega^*_s(L_{s1}i_{qs1} + \tau_r\phi^*_{rd}\omega^*_{sl})\right\} \\ \dot{e}_5 = \dot{i}^*_{qs2} - \frac{1}{L_{s2}}\left\{v_{qs2} - R_{s2}i_{qs2} - \omega^*_s(L_{s2}i_{ds2} + \phi^*_{rd})\right\} \\ \dot{e}_6 = \dot{i}^*_{ds2} - \frac{1}{L_{s2}}\left\{v_{ds2} - R_{s2}i_{ds2} + \omega^*_s(L_{s2}i_{qs2} + \tau_r\phi^*_{rd}\omega^*_{sl})\right\} \end{cases} \tag{39}$$

The final Lyapunov function and its derivative can be given as follows:

$$v_2 = \frac{1}{2}(e_1^2 + e_2^2 + e_3^2 + e_4^2 + e_5^2 + e_6^2) \tag{40}$$

$$\dot{v}_2 = e_1\,\dot{e}_1 + e_2\,\dot{e}_2 + e_3\,\dot{e}_3 + e_4\,\dot{e}_4 + e_5\,\dot{e}_5 + e_6\,\dot{e}_6 \tag{41}$$

By applying Lyapunov's stability theorem as in the first step, where the derivative of v_2 must always be negative ($v_2 < 0$), in this case, we take:

$$\begin{cases} \dot{e}_3 = -k_3 e_3 \\ \dot{e}_4 = -k_4 e_4 \\ \dot{e}_5 = -k_5 e_5 \\ \dot{e}_6 = -k_6 e_6 \end{cases} \tag{42}$$

where k_3,k_4,k_5, and k_6 are positive constants,

From the system of Eqs. (39) and (42), we find the actual control represented by the following equations:

$$\begin{cases} v_{qs1}^{*} = L_{s1}\left[k_3 e_3 - \rho_1 + \dot{i}_{qs1}^{*}\right] \\ v_{ds1}^{*} = L_{s1}\left[k_4 e_4 - \rho_2 + \dot{i}_{ds1}^{*}\right] \\ v_{qs2}^{*} = L_{s2}\left[k_5 e_5 - \rho_3 + \dot{i}_{qs2}^{*}\right] \\ v_{ds2}^{*} = L_{s2}\left[k_6 e_6 - \rho_4 + \dot{i}_{ds2}^{*}\right] \end{cases} \tag{43}$$

with:

$$\begin{cases} \rho_1 = \frac{1}{L_{s1}}\left\{-R_{s1} i_{qs1} - \omega_s^{*}(L_{s1} i_{ds1} + \varphi_{rd}^{*})\right\} \\ \rho_2 = \frac{1}{L_{s1}}\left\{-R_{s1} i_{ds1} + \omega_s^{*}(L_{s1} i_{qs1} + \tau_r \varphi_{rd}^{*} \omega_{sl}^{*})\right\} \\ \rho_3 = \frac{1}{L_{s2}}\left\{-R_{s2} i_{qs2} - \omega_s^{*}(L_{s2} i_{ds2} + \varphi_{rd}^{*})\right\} \\ \rho_4 = \frac{1}{L_{s2}}\left\{-R_{s2} i_{ds2} + \omega_s^{*}(L_{s2} i_{qs2} + \tau_r \varphi_{rd}^{*} \omega_{sl}^{*})\right\} \end{cases} \tag{44}$$

Notice that the WT-DSIG system will become stable only when the PI gains (i.e., $k_{p\text{-}\Omega}$, $k_{p\text{-}\phi}$, $k_{p\text{-}is}$, $k_{i\text{-}\Omega}$, $k_{i\text{-}\phi}$, $k_{i\text{-}is}$), or the BS gains (i.e., k_1, k_2, k_3, k_4, k_5, and k_6) are optimally chosen. The SABO algorithm is used in this paper to achieve this objective.

4 SABO algorithm

In this section, the operating principle and modeling of the suggested SABO algorithm are presented.

4.1 Algorithm initialization

For any given optimization problem, the search space is the space where the optimal solution belongs. In addition, the number of variables in the given problem equals the dimension space, which is a subset within the search space. Population members or algorithm searcher agents choose the values for the decision variables based on where they are in the search space. As a result, a vector known as the decision variables is considered to mathematically represent each search agent. The population of the algorithm is the whole collection of search agents. A matrix is used to depict the population of the method (45) numerically. Equation (46) randomly initializes the principal locations of the search agents within the search space [29].

$$X = \begin{bmatrix} X_1 \\ \cdot \\ \cdot \\ \cdot \\ X_i \\ \cdot \\ \cdot \\ \cdot \\ X_N \end{bmatrix}_{N\times m} = \begin{bmatrix} x_{1,1} & \cdots & x_{1,d} & \cdots & x_{1,m} \\ \cdot & \cdot & \cdot & \cdot & \cdot \\ \cdot & \cdot & \cdot & \cdot & \cdot \\ \cdot & \cdot & \cdot & \cdot & \cdot \\ x_{i,1} & \cdots & x_{i,d} & \cdots & x_{i,m} \\ \cdot & \cdot & \cdot & \cdot & \cdot \\ \cdot & \cdot & \cdot & \cdot & \cdot \\ \cdot & \cdot & \cdot & \cdot & \cdot \\ x_{N,1} & \cdots & x_{N,d} & \cdots & x_{N,m} \end{bmatrix}_{N\times m} \tag{45}$$

$$x_{i,d} = lb_d + r_{i,d}.(ub_d - lb_d),\ i = 1, \ldots, N,\ d = 1, \ldots, m, \tag{46}$$

where m and N are the numbers of the problem variables and search members, $r_{i,d}$ is a random integer in the interval [0, 1], and ub_d and lb_d are the upper bound and lower bound of the dth problem variable, respectively. The algorithm's most crucial component is the population matrix of the SABO, X, which contains the ith search agent (population member).

Each search agent represents a possible solution and advises decision variables' values. This means that the problem's objective function is evaluated using each search agent. According to Eq. (47), a vector $\vec{F}$ is employed to represent the evaluated values of the objective function. Depending on where each member of the population enters the prescribed values for the problem's choice variables, the objective function is evaluated and recorded in the vector $\vec{F}$. As a result, the element count of the vector $\vec{F}$ and the membership count N of the population is identical.

$$\vec{F} = \begin{bmatrix} F_1 \\ \cdot \\ \cdot \\ \cdot \\ F_i \\ \cdot \\ \cdot \\ \cdot \\ F_N \end{bmatrix}_{N\times 1} = \begin{bmatrix} F(X_1) \\ \cdot \\ \cdot \\ \cdot \\ F(X_i) \\ \cdot \\ \cdot \\ \cdot \\ F(X_N) \end{bmatrix}_{N\times m} \tag{47}$$

F_i is the objective function's evaluated value based on the ith search member and $\vec{F}$ is the vector with the objective function's values.

The objective function's evaluated values serve as appropriate benchmarks for assessing the search agents' output caliber. Consequently, the best value discovered for the goal function stands for the optimal search agent. Similarly, the poorest search agent is the worst value obtained for the goal

function. Finding and keeping the best search agent process continues until the algorithm reaches the final iteration.

4.2 Mathematical modeling of SABO

The SABO is constructed based on three mathematical concepts, including averages, variations in search agent positions, and the sign of the error among the two target values function. An easy way to update all search agents' positions (the generation of all the population members of the $(t+1)$th iteration) is to utilize the arithmetic mean location of all search agents, i.e., the tth iteration's population members, rather than just employing, e.g., the location of the worst or best search agent. However, the SABO's method of calculating the arithmetic mean is distinct as it relies on a specific operation (known as v-subtraction), defined by:

$$SA -_v SB = sign(F(SA) - F(SB))\left(SA - \vec{v} * SB\right) \tag{48}$$

where $\vec{v}$ is an m-dimension vector, the sign is the signum function, and the objective functions' values of the search agents SA and SB are represented by $F(SA)$ and $F(SB)$, respectively. The symbol " $*$ " indicates the Hadamard product of the two vectors, meaning that every element of the final vectors is created by multiplying the respective elements of the original two vectors. Given that the definition of the v-subtraction employs a random vector $\vec{v}$ with elements from the set {1,2}, it is crucial to remember that the operation's result is the points in a subset of the search space with a cardinality of 2^{m+1}.

The arithmetic mean of the v-subtraction of each search agent $X_j, j = 1, 2, \ldots, N$, from the search agent X_i, determines the displacement of each search agent X_i in the search space in the proposed SABO. Consequently,(49) gives each search agent's new position.

$$X_i^{new} = X_i + \vec{r}_i * \frac{1}{N}\sum_{j=1}^{N}\left(X_i -_v X_j\right),\ i = 1, 2, \ldots, N, \tag{49}$$

where $\vec{r}_i$ is a vector with dimension m, X_i^{new} is the new recommended location for the i^{th} search agent X_i. The components of this vector have normal distributions with values falling between [0, 1].

Then, by (50), this suggested new position is accepted as the new location of the relevant agent if it improves the value of the objective function.

$$X_i = \begin{cases} X_i^{\text{new}}, & F_i^{\text{new}} < F_i; \\ X_i, & else, \end{cases} \tag{50}$$

where F_i and F_i^{new} represent the search agents X_i and X_i^{new} respective objective function values.

Since we can rewrite (49) in the form $X_i^{new} = X_i + \vec{r}_i * \vec{M}_i$, we can view it as the motion equation of the search agent X_i. The direction of the search agent's movement X_i to its new position X_i^{new} is determined by the mean vector $\vec{M}_i = \frac{1}{N}\sum_{j=1}^{N}\left(X_i -_v X_j\right) = \frac{1}{N}\sum_{j=1}^{N}\vec{\chi}_{ij}$, which is represented by the v-subtraction $X_i -_v X_j$. The ability of the search mechanism described in (49) to efficiently complete the exploitation and exploration phases in order to identify the most promising locations within the search space is its essential characteristic. The operations of "v-subtraction" (i.e., the vector $\vec{\chi}_{ij}$) and "arithmetic mean of the v-subtractions" (i.e., the vector $\vec{M}_i$) are used to realize the exploration and exploitation phases, respectively, as illustrated in Figs. 4a, b.

4.3 Repetition process and flowchart

When all search agents are updated, the algorithm's first iteration is complete. Then, the algorithm goes to the next iteration with the freshly determined values for the search agent and goal function placements. The best candidate solution up to that moment is stored as the most optimum search agent for each cycle. As shown by steps (46) through (50), the search agents are updated until the last algorithmic iteration. The most ideal candidate solution stored throughout the algorithm's iterations is chosen to provide the ultimate solution to the problem. The flowchart that shows the steps required in putting the SABO into practice is shown in Fig. 5.

4.4 Application of the SABO for PI and BS parameters tuning

The SABO is applied to tune the PI and BS controllers' parameters. In the two cases, the sum of the ITAEs between the actual speed, flux, and stators currents' and their desired references is considered as the objective function to be minimized, which can be defined as follows:

$$\begin{aligned} \min(Obj) = &\int_0^t t.\left(\Omega_{mec}^* - \Omega_{mec}\right)\,dt \\ &+ \int_0^t t\cdot\left(\phi_{rd}^* - \phi_{rd}\right)dt + \int_0^t t\cdot\left(i_{ds1}^* - i_{ds1}\right)dt \end{aligned} \tag{51}$$

The population size, number of iterations, and boundaries of the variables to be optimized are defined in Table 1. The parameters to be optimized are:

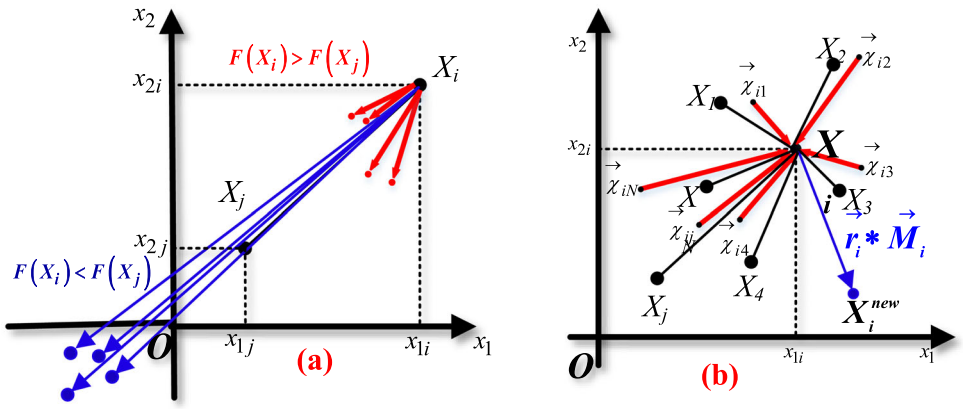

Fig. 4 Schematic diagram of the exploration phase considering for $m = 2$; **a** "v-subtractions" and **b** "arithmetic of the v-subtraction"

Table 1 SABO Parameters

Parameters	Controller	Values
Number of variables	PI	3; [$\omega_{n\text{-}\Omega mec}\omega_{\text{n-}\phi rd}\omega_{n\text{-}is1,2}$]
Population size		15
Maximum iteration		5
Lower bound		[100 10 1000]
Upper bound		[700 100 3000]
Number of variables	BS	3; [$k_1k_2k_3$]
Population size		15
Maximum iteration		5
Lower bound		[4000 3000 20000]
Upper bound		[10000 8000 40000]

- The natural frequencies of the speed, flux, and stators currents, $\omega_{n\text{-}\Omega\text{mec}}$, $\omega_{n\text{-}\varphi rd}$, and $\omega_{n\text{-}is1,2}$, respectively, in the case of the PI regulator.
- The gains k_1-k_6 of the speed, flux, and stators currents, respectively, in the case of the BS controller.

Through simulations in MATLAB, considering the average model of the whole system, the SABO is introduced to attain the required parameters of the PI and BS controllers offline while considering each controller's impact on the others. Table 4 in the Appendix lists the system's parameters used in this simulation. Table 2 summarizes the optimal values of the PI natural frequencies and BS gains with those computed by the trial-and-error tuning method.

5 Hardware-in-the-loop results

Hardware-in-the-loop (HIL) implementation using RT-BOX involves integrating real-time simulation with physical hardware components to test and validate control systems safely and efficiently. The real-time simulator RT-BOX is a powerful interface between the simulation environment and the actual hardware. In a typical HIL setup with RT-BOX, the system under test (such as a controller) interacts with a simulated environment that runs in real-time on the RT-BOX. The RT-BOX simulates the dynamics of the plant or system that the controller is designed to manage. It continuously exchanges data with the physical controller, providing realistic feedback as if controlling a natural system. This setup allows engineers to test control algorithms and hardware in real-world conditions, thereby saving costs that would have been associated with full-scale physical testing. RT-BOX is particularly valued in fields like automotive, aerospace, and renewable energy, where testing in actual environments can be dangerous, expensive, or impractical. Using HIL with RT-BOX, engineers can validate their designs, uncover potential issues, and refine their systems before deploying them in the field, thus reducing development time and improving overall system reliability.

Based on the Plecs/RT-Box platform, the performance of the proposed control approach implemented for a 1.5 MW rated capacity DSIG within a wind turbine system is evaluated, as shown in Fig. 6. A comparative study assessing the effectiveness of the proposed optimized controllers with the conventional ones is carried out under variable wind speed profile. The DSIG's nominal characteristics are given in Table 4, with the optimal controllers' parameters of Table 2 and for a sampling time $T_s = 2 \times 10^{-5}$. Note that in the system of Fig. 6, the analog outputs define the system measurements to be provided to the control stage as analog inputs. The switches' commands are sent from the control stage to the plant using PWM out to PWM capture.

The obtained results are presented in Figs. 7, 8, 9, 10, 11, 12, 13, 14, 15, 16, 17, 18 showing the reported controllers' performance in response to the imposed wind speed profile. These figures display for each controller the rotor speed, electromagnetic torque, direct rotor flux, direct and quadrature of the stator #1 current, a-phase currents of the stators #1 and

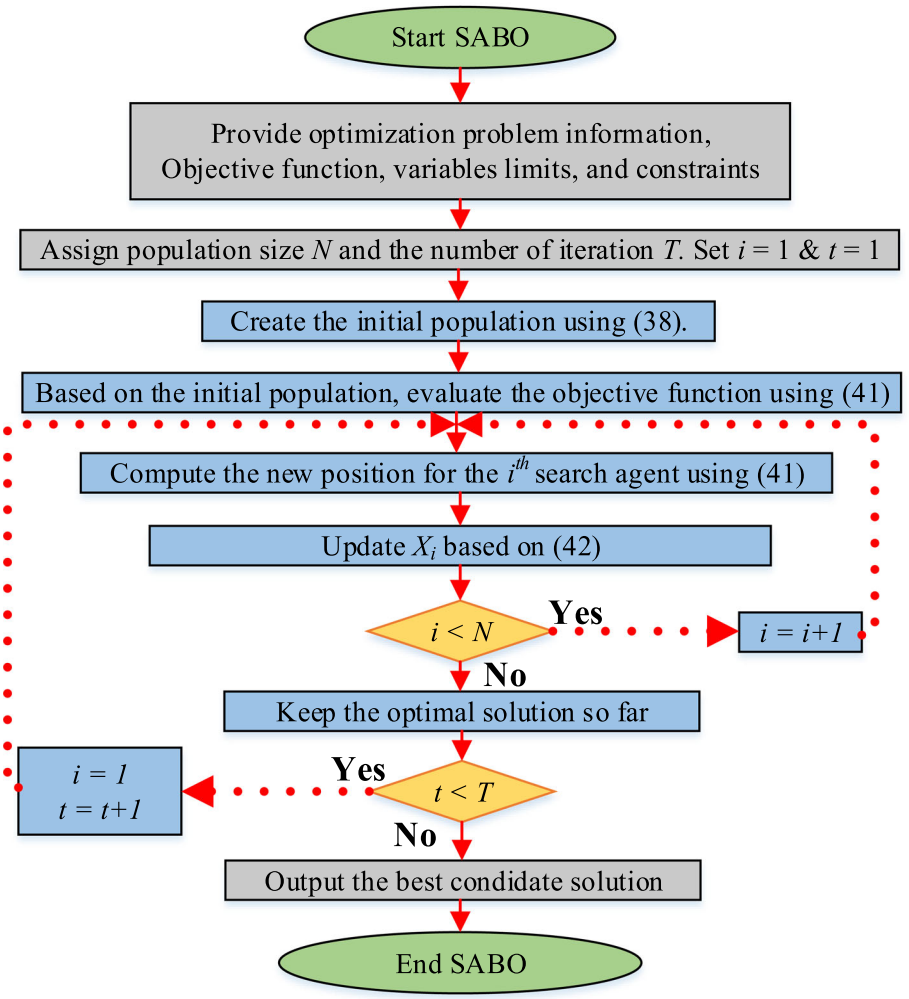

Fig. 5 Flowchart of the SABO algorithm

Table 2 PI and BS controllers' gains and performance of the tuned controllers

Tuning method	Controller	Gains	ITAEs				
		Rotor speed control	Rotor flux control	Stators currents control	$\Delta e_{\Omega mec}$	$\Delta e_{\phi rd}$	Δe_{ids1}
Trial and error	PI	$\omega_{n\text{-}\Omega mec} = 600$	$\omega_{n\text{-}\phi rd} = 65$	$\omega_{n\text{-}is1,2} = 2000$	0.3802	0.0278	23.3987
	BS	$k_1 = 2000$	$k_2 = 5000$	$k_{3\text{-}6} = 30{,}000$	0.1058	0.1464	8.4616
SABO	PI	$\omega_{n\text{-}\Omega mec} = 402.123$	$\omega_{n\text{-}\phi rd} = 48.10$	$\omega_{n\text{-}is1,2} = 2227.17$	0.0248	0.6747	7.2567
	BS	$k_1 = 2.3424e+3$	$k_2 = 8.8016e+3$	$k_{3\text{-}6} = 1.8747e+4$	0.0626	0.0247	0.0569

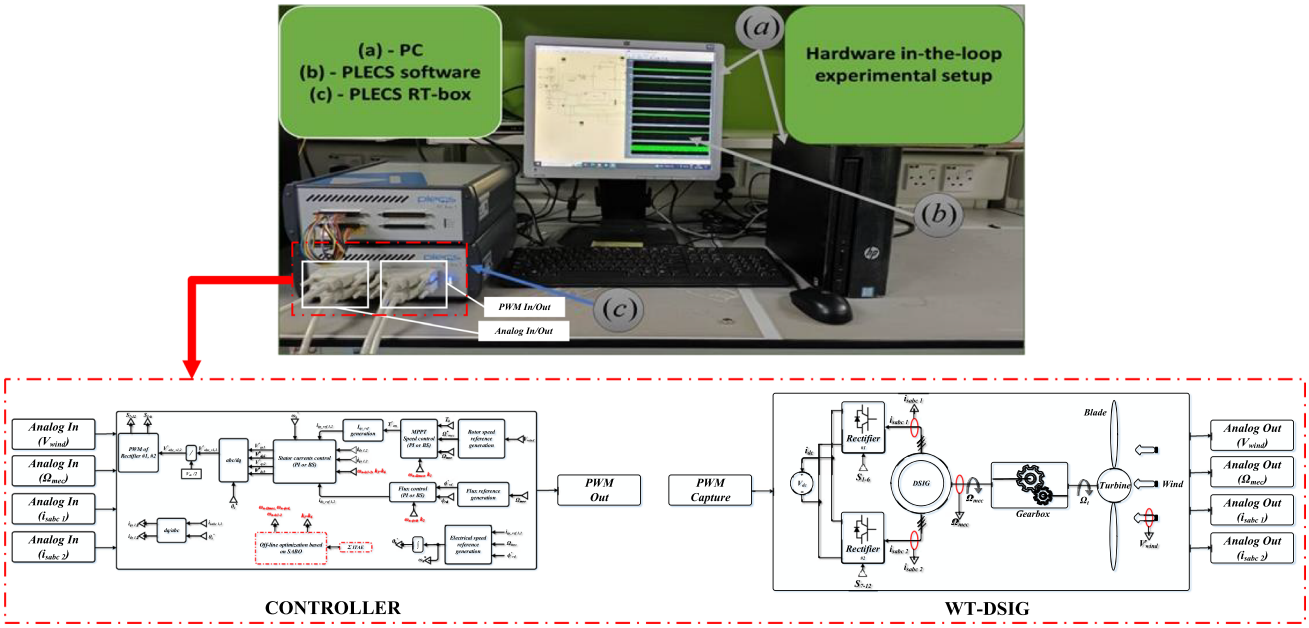

Fig. 6 Hardware-in-the-loop experimental setup

Table 3 Time-integral performance criteria and THD for different controllers

Tuning method		PI						BS						THD_{PI}%	THD_{BS}%
		Ω_{mec}	ϕ_{rd}	i_{ds1}	i_{qs1}	i_{ds2}	i_{qs2}	Ω_{mec}	ϕ_{rd}	i_{ds1}	i_{qs1}	i_{ds2}	i_{qs2}	i_{as1}	i_{as1}
Trial–error	ISE	0.19	0.18	$3e^5$	$8e^5$	$3e^5$	$8e^5$	0.18	0.12	$2e^5$	$7e^5$	$2e^5$	$7e^5$	3.3456%	2.8665%
	IAE	2.1	0.2	$3e^3$	$5e^3$	$3e^3$	$5e^3$	2	0.15	$3e^3$	$4e^3$	$3e^3$	$4e^3$		
SABO	ISE	0.16	0.17	$3e^5$	$4e^5$	$3e^5$	$4e^5$	0.14	0.12	$2e^5$	$3e^5$	$2e^5$	$3e^5$	0.8103%	0.5047%
	IAE	2	0.2	$3e^3$	$4e^3$	$3e^3$	$4e^3$	1	0.1	$3e^3$	$4e^3$	$3e^3$	$4e^3$		

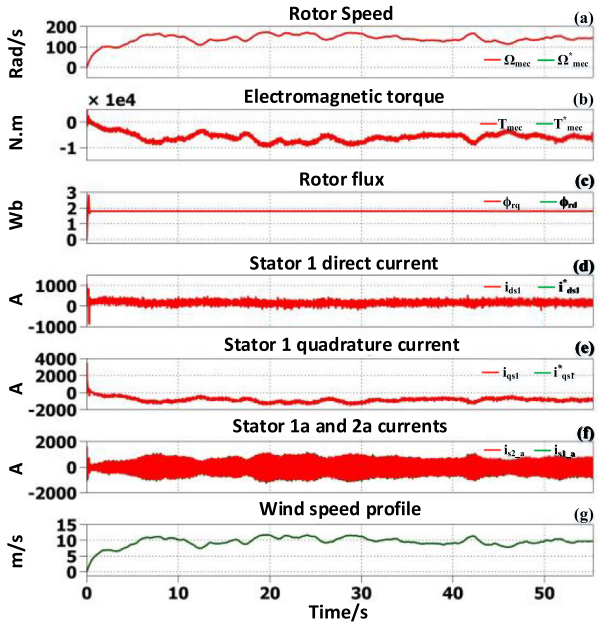

Fig. 7 HiL results for variable wind with the conventional PI regulator

#2, and their references. In addition, the zoom-in at transient and steady states and the wind profile are also depicted in these figures. Moreover, the time-integral performance criteria, IAE and ISE, as well as the THD corresponding to each controller, are listed in Table 3.

Based on these figures and Table 3, the following observations are made:

- All the designed controllers ensure the measured speed, electromagnetic torque, and stators' currents of the DSIG following the wind profile, while the rotor flux remains constant.
- The optimized PI controller provides better transient and steady-state performance with the least IAE and ISE errors than the conventional PI regulator as Figs. 9–12 show and Table 3 highlights. More particularly, by using the optimized controllers, the actual speed, electromagnetic torque, flux, and stator #1 current *dq* components accurately track their references' average values (see Fig. 10a–e) with low ripples at steady state. When using the

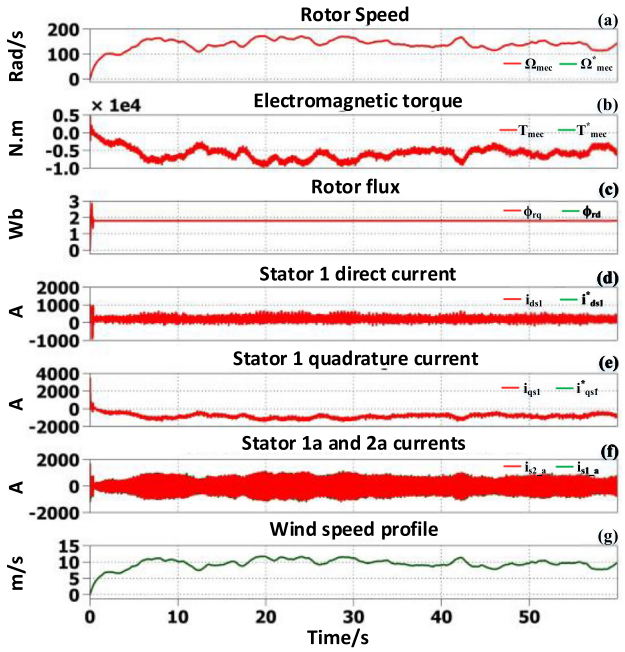

Fig. 8 HiL results for variable wind with the optimized PI regulator

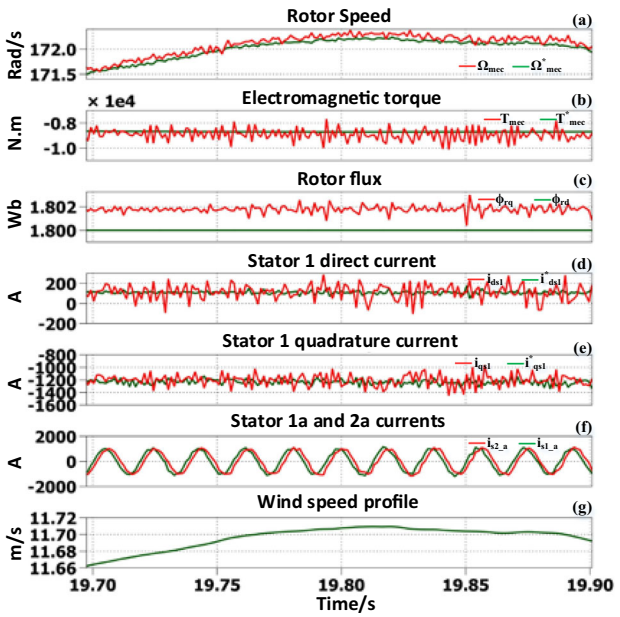

Fig. 9 Steady-state performance: HiL results zoom in

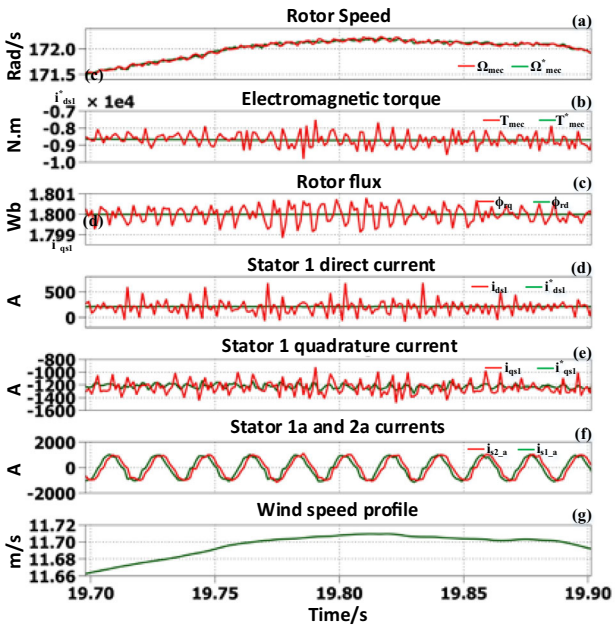

Fig. 10 Steady-state performance: HiL results zoom in

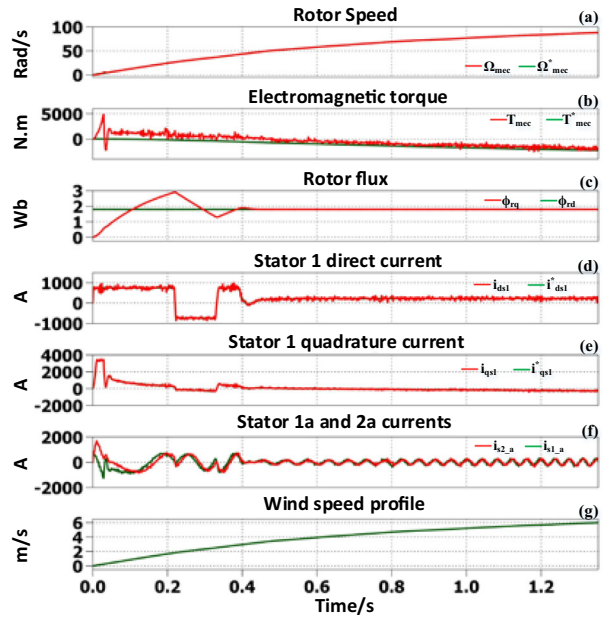

Fig. 11 Zoom in transient response HiL results

traditional controllers, significant ripples and steady-state errors are observed among the actual speed, electromagnetic torque, and flux, as Fig. 9a–c depicts.

- The optimized PI controller provides fast transient responses with settling time, t_s, about 0.3 s compared to the traditional PI with t_s of around 0.4 s, as Figs. 11 and 12 demonstrate.
- Similarly, the BS controller with optimized parameters shows excellent performance regarding fast dynamic responses, teeny ripples at steady state, and low IAE and ISE errors compared to the traditional BS. The performance enhancement can be noticed from Figs. 15 and 16, the actual speed, electromagnetic torque, flux, and stator #1 current *dq* components track their references with high accuracy and a settling time of around 0.1 s.

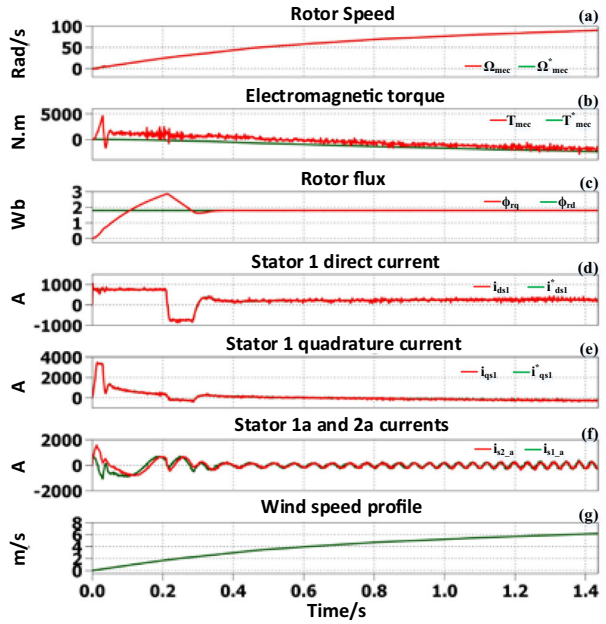

Fig. 12 Zoom in transient response HiL results

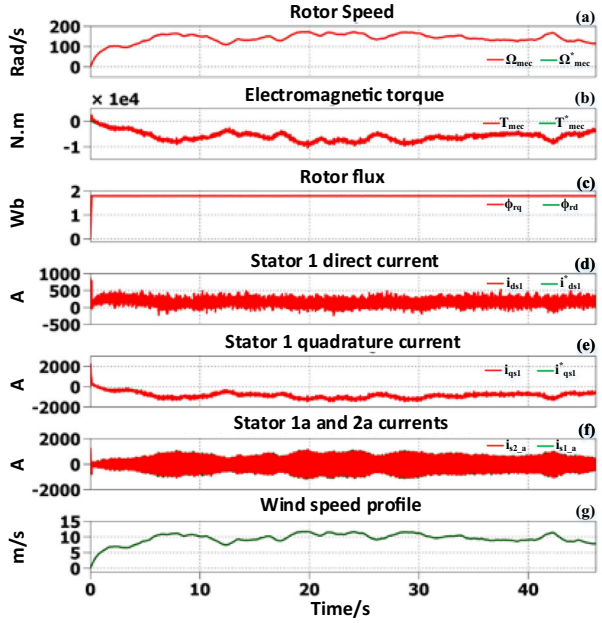

Fig. 14 HiL results for variable wind with the optimized backstepping regulator

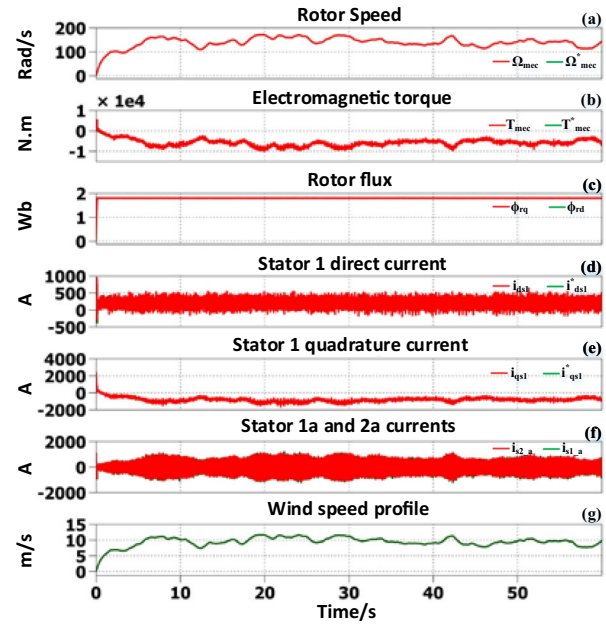

Fig. 13 HiL results for variable wind with the backstepping regulator

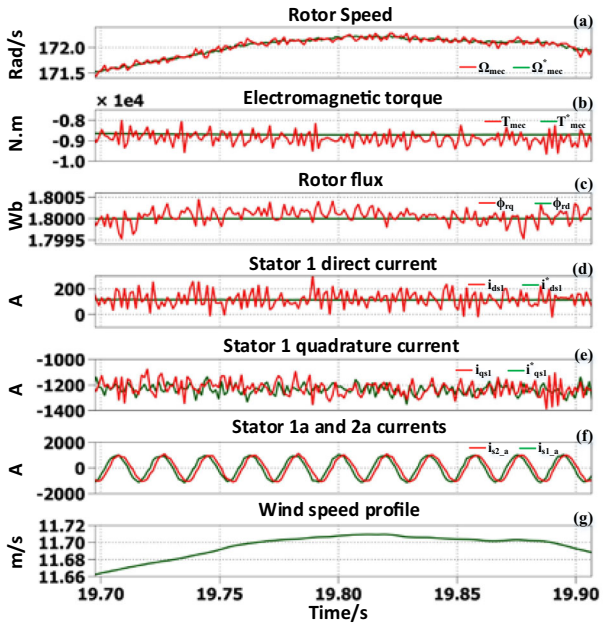

Fig. 15 Steady-state performance: HiL results Zoom in

- The optimized BS controller offers the best transient response time and lowest steady-state ripples and static errors compared to the optimized PI controller. In addition, the traditional BS is better than the optimized PI regarding the transient response time, but the optimized PI controller has superior steady-state performance.

Sinusoidal waveforms of the phase stators currents with high quality are obtained based on the optimized regulators, with a noticeable reduction of the THD values, 0.8103% for the PI and 0.5047% for BS, compared to the traditional ones with high THDs, 3.3456% for PI and 2.8665% for BS.

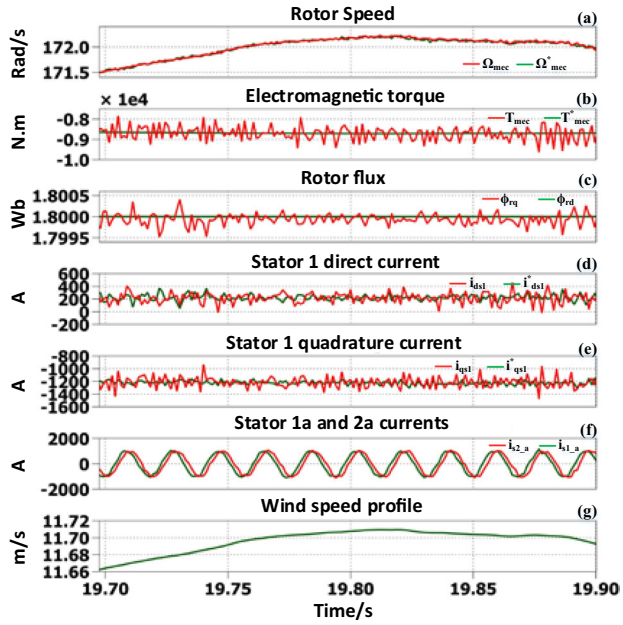

Fig. 16 Steady-state performance: HiL results Zoom in

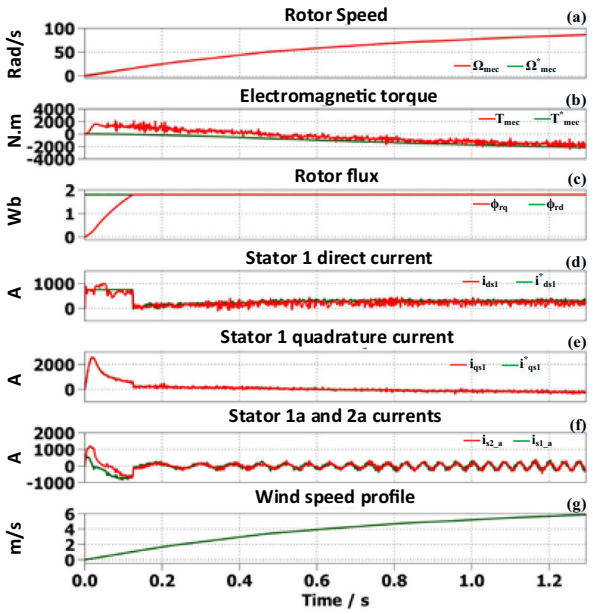

Fig. 17 Zoom in transient response HiL results

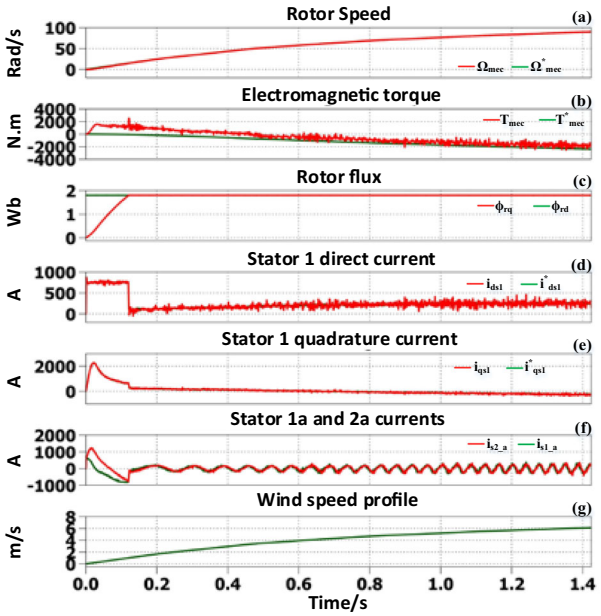

Fig. 18 Zoom in transient response HiL results

6 Conclusion

This paper proposes a new optimization technique to optimally tune the PI/BS controllers incorporating FOC for a WT-DSIG system. The performance of the designed controllers is investigated against the conventional controllers through HIL tests using the RT-Box platform. The results demonstrate that the proposed optimal control approach ensures high tracking performance of the desired references with enhanced transient and steady-state responses and comparatively low IAE and ISE errors under a variable wind speed profile. In addition, the optimally designed controllers significantly improve the THD of the stators currents with 0.8103% for PI and 0.5047% for BS, compared to the traditional ones with 3.3456% for PI and 2.8665% for BS. It is concluded that the PI and BS controllers with optimally tuned parameters show superior performance compared to the traditional ones in terms of fast transient response, less error, and low ripples during steady-state operation.

Appendix

This appendix provides the parameters of the simulated system.

See Table 4.

Table 4 Wind turbine system parameters [1]

Quantity	Values
Attenuation factor on the rotor	$\gamma = 0.25375$
Average wind speed	$V_{moy} = 8.12$ m.s^{-1}
Turbine's radius	$R = 32$ m
Gain of the gearbox	$G = 58$
Coefficient of maximum power	$C_{pmax} = 0.47$
Optimal relative wind velocity	$\lambda_{opt} = 8.1$
Nominal power of DSIG	$P_n = P_{max} = 1.5$ MW
Voltage (RMS)	$E = 400$ V
Pole pairs number	$P = 2$
Resistance of the stator	$R_{s1} = R_{s2} = 0.008\ \Omega$
Inductance of the stator	$L_{s1} = L_{s2} = 0.134$ mH
Magnetizing inductance	$L_m = 0.0045$ H
Resistance of the rotor	$R_r = 0.007\ \Omega$
Inductance of the rotor	$L_r = 0.067$ mH
Moment of inertia	$J = 10$ kg.m^2
Coefficient of viscous	$k_f = 0.0015$ Nm s/rd
Impedance of the smoothing choke	$X = 0.314$

Author contributions Khaled Benzaoui and Ahmed Bendib contributed to analysis and/or interpretation of data and conception and design of study. Khaled Benzaoui contributed to acquisition of data. Ahmed Bendib and Ahmed Elsanabary drafted and revised the manuscript critically for important intellectual content.

Data availability No datasets were generated or analyzed during the current study.

Declarations

Conflict of interest The authors declare no competing interests.

References

1. Ghoudelbourk S, Dib D, Omeiri A, Azar AT (2016) MPPT control in wind energy conversion systems and the application of fractional control (PI$^{\alpha}$) in pitch wind turbine. IJMIC 26(2):140. https://doi.org/10.1504/IJMIC.2016.078329
2. Miryousefi Aval SM, Ahadi A, Hayati H (2016) A novel method for reliability and risk evaluation of wind energy conversion systems considering wind speed correlation. Front Energy 10(1):46–56. https://doi.org/10.1007/s11708-015-0384-4
3. Mahboub MA, Drid S, Sid MA, Cheikh R (2017) Sliding mode control of grid connected brushless doubly fed induction generator driven by wind turbine in variable speed. Int J Syst Assur Eng Manag 8(S2):788–798. https://doi.org/10.1007/s13198-016-0524-1
4. Tiwari R, Babu NR (2016) Recent developments of control strategies for wind energy conversion system. Renew Sustain Energy Rev 66:268–285
5. Hossain MM, Ali MH (2015) Future research directions for the wind turbine generator system. Renew Sustain Energy Rev 49(481–489):2015
6. Ameur F, Kouzi K, Merzouk NK (2016) Design and analysis of direct power and flux control of dual stator induction generator integrated in wind conversion system connected to the grid. Electrotehnica, Electronica, Automatica, 64(3), Accessed: Dec. 28, 2023. https://search.ebscohost.com/login.aspx
7. Lekhchine S, Bahi T, Soufi Y (2014) Indirect rotor field oriented control based on fuzzy logic controlled double star induction machine. Int J Electric Power & Energy Syst. 57:206–211
8. Gutiérrez-Escalona J, Roncero-Clemente C, González-Romera E, Milanés-Montero MI, Husev O, Romero-Cadaval E (2023) PV-battery assisted three-level T-type inverter for AC residential nanogrid realized with small-scale HIL Units. IEEE Access, 2023, Accessed: Dec. 28, 2023. https://ieeexplore.ieee.org/abstract/document/10124216/
9. Ameur F, Kouzi K (2014) Optimized PI and fuzzy speed vector control of dual stator induction generator used in a variable speed wind. Int J Electric Energy 2(1):74–81
10. Bouyahia O, Betin F, Yazidi A (2022) Optimal sliding mode control of a symmetrical six-phase induction generator for wind turbines. IEEE Trans Ind Appl 58(6):7308–7317
11. Benakcha M, Benakcha A, Ammar A (2022) Backstepping sliding mode control of DSIG driven by variable speed wind turbine. In 2022 19th International multi-conference on systems, signals & devices (SSD), IEEE, 2022, pp. 296–302. Accessed: Jun. 15, 2024. https://ieeexplore.ieee.org/abstract/document/9955775/
12. Guettab A, Bounadja E, Boudjema Z, Taleb R (2023) Third-order super-twisting control of a double stator asynchronous generator integrated in a wind turbine system under single-phase open fault. Circuit Theory & Apps 51(4):1858–1878. https://doi.org/10.1002/cta.3511
13. Guettab A, Boudjema Z, Bounadja E, Taleb R (2022) Improved control scheme of a dual star induction generator integrated in a wind turbine system in normal and open-phase fault mode. Energy Rep 8:6866–6875
14. Abdulwahab I, Abubakar AS, Olaniyan A, Sadiq BO, Faskari SA (2022) Control of dual stator induction generator based wind energy conversion system. In 2022 IEEE Nigeria 4th international conference on disruptive technologies for sustainable development (NIGERCON), IEEE, 2022, pp. 1–5. Accessed: Jun. 15, 2024. https://ieeexplore.ieee.org/abstract/document/9803100/
15. Mesai-ahmed H, Bentaallah A, Cardoso AJM, Djeriri Y, Jlassi I (2021) Robust neural control of the dual star induction generator used in a grid-connected wind energy conversion system. Math Model Eng Problems, 8(3). Accessed: Jun. 15, 2024. https://www.academia.edu/download/88275290/55764
16. Chekkal S, Aouzellag D, Ghedamsi K, Amimeur H (2011) New control strategy of wind generator based on the dual-stator induction generator. In: 2011 10th International conference on environment and electrical engineering, IEEE, 2011, pp. 1–4. Accessed: Jun. 15, 2024. https://ieeexplore.ieee.org/abstract/document/5874593/
17. Liu H, Bu F, Huang W, Qin H, Tan Y, Qian Z (2022) Linear active disturbance rejection control for dual-stator winding induction generator AC power system. IEEE Trans Ind Electron 70(7):6597–6607
18. Bu F, Liu H, Huang W, Shi J, Liu Z, Sun T, Qin H, Luo Z, Deaconu SI (2024) Dynamic-decoupled current control based on reduced-order observer for dual stator-winding induction generator. IEEE J Emerg Selected Topics in Power Electron, 2023, Accessed: Jun. 15, 2024. https://ieeexplore.ieee.org/abstract/document/10359158/
19. Abdolghani N, Milimonfared J, Abedi M, Zamani MH (2021) Improving transient stability of dual stator-winding induction

generator-based wind farms by slip frequency control. IEEE J Emerg Selected Topics in Power Electron 9(5):5354–5366
20. Benakcha M, Benalia L, Tourqui DE, Benakcha A (2018) Backstepping control of dual stator induction generator used in wind energy conversion system. Int J Renew Energy Res 8(1):384–395
21. Benakcha M, Benalia L, Ammar A, Bourek A (2019) Wind energy conversion system based on dual stator induction generator controlled by nonlinear backstepping and pi controllers. Int J Syst Assur Eng Manag 10(4):499–509. https://doi.org/10.1007/s13198-018-0734-9
22. Hamitouche K, Chekkal S, Amimeur H, Aouzellag D (2020) A new control strategy of dual stator induction generator with power regulation. Journal Européen des Systèmes Automatisés 53(4):469–478
23. Ameur F, Kouzi K (2013) Genetic algorithm optimized PI and fuzzy logic speed vector control of dual stator induction generator in wind energy conversion system. In 3rd International Conference on Systems and Control, IEEE, 2013, pp. 1036–1042. Accessed: Jun. 15, 2024. https://ieeexplore.ieee.org/abstract/document/6750982/
24. Slootweg JG, Polinder H, Kling WL (2003) Representing wind turbine electrical generating systems in fundamental frequency simulations. IEEE Trans Energy Convers 18(4):516–524
25. Morren J, Pierik J, De Haan SW (2006) Inertial response of variable speed wind turbines. Electric Power Syst Res 76(11):980–987
26. Hosseinabadi PA, Pota H, Mekhilef S, Schwartz H (2023) Fixed-time observer-based control of DFIG-based wind energy conversion systems for maximum power extraction. Int J Electr Power Energy Syst 146:108741
27. Ahmad I, M'zoughi F, Aboutalebi P, Garrido I, Garrido AJ (2023) Fuzzy logic control of an artificial neural network-based floating offshore wind turbine model integrated with four oscillating water columns. Ocean Eng 269:113578
28. El Aimani S (2004) Modélisation des différentes technologies d'éoliennes intégrées dans un réseau de moyenne tension. These de doctorat, Ecole Centrale de Lille, 2004. Accessed: Jun. 25, 2024. https://theses.fr/2004ECLI0004
29. Trojovský P, Dehghani M (2023) Subtraction-average-based optimizer: a new swarm-inspired metaheuristic algorithm for solving optimization problems. Biomimetics 8(2):2. https://doi.org/10.3390/biomimetics8020149